

Multiaxial Validation of a Magneto-Elastic Vector-Play Model

Luiz Guilherme da Silva^{1,2,3}, Laurent Bernard³, Florian Martin⁴,
Anouar Belahcen⁴, and Laurent Daniel^{1,2}

¹CentraleSupélec, CNRS, Laboratoire de Génie Electrique et Electronique de Paris, Université Paris-Saclay, 91192 Gif-sur-Yvette, France

²CNRS, Laboratoire de Génie Electrique et Electronique de Paris, Sorbonne Université, 75252 Paris, France

³GRUCAD/EEL/CTC, Federal University of Santa Catarina, Florianópolis 88040-900, Brazil

⁴Department of Electrical Engineering and Automation, Aalto University, 00076 Espoo, Finland

The ferromagnetic materials used in electrical machines are usually subjected to multiaxial mechanical loadings. The influence of these multiaxial stress states on the hysteresis behavior can be modeled using an extended vector-play model. In this approach, a combination of an anhysteretic multiscale model and a magnetic hysteresis vector-play model is proposed. The magnetic hysteresis response of a nonoriented (NO) iron–silicon steel subjected to biaxial stress loadings is simulated using the vector-play approach. By considering a simplified texture, anisotropy effects are also taken into account. The simulation results are then compared with experimental measurements previously presented in the literature. It is shown that the proposed approach, with parameters identified from uniaxial measurements along one direction only, allows predicting the hysteresis losses under bi-tension, bi-compression, and shear with errors lower than 15% when the field is along rolling direction (RD). The hysteresis losses for a more challenging configuration, with field along the transverse direction (TD) and under biaxial stress, are also reasonably predicted with errors lower than 25%.

Index Terms— Anisotropy, magnetic hysteresis, magneto-elasticity, multiaxial stress, multiscale modeling, nonoriented (NO) iron–silicon.

I. INTRODUCTION

THE ferromagnetic materials used in electrical machines are sensitive to mechanical stress [1], [2]. The magneto-mechanical coupling is notably observed in the influence of the stress state on the behavior of ferromagnetic materials (permeability and losses) [3], [4], [5], [6], [7], [8], and in the efficiency of electromagnetic devices [9], [10], [11]. The sources of mechanical stress in electrical machines are remarkably due to manufacturing processes [12], [13] and centrifugal forces of high-speed machines [11], [14]. Therefore, the ferromagnetic materials are subjected to multiaxial stress states.

Experimental benches devoted to the characterization of magnetic materials under biaxial stress are presented in [15], [16], [17], [18], and [19]. It is observed that pure shear [with compression applied in the rolling direction (RD) and tension in the transverse direction (TD)] strongly increases the hysteresis losses [20], [21] and degrades the secant permeability [17] of nonoriented (NO) Fe–Si when the magnetization is along the RD. The magnetostriction strain of low-carbon steel is also sensitive to biaxial stress states [22].

A common approach to modeling the coupled magneto-elastic behavior is the extension of classical magnetic hysteresis models. An extension of the Jiles–Atherton–Sablik approach [23] to the case of biaxial mechanical loadings is presented in [24] and [25]. Two uniaxial magneto-mechanical

energies are introduced corresponding to the stresses applied along two perpendicular axes. A fictitious magnetic field mimics the effects of mechanical stress on the magnetic behavior, and it is further added to an effective magnetic field. Because the reversible behavior is defined as a function of the effective field, thermodynamic inconsistency is found in Jiles–Atherton models, as pointed out in [26]. Moreover, the approach presented in [24] is limited to in-plane stress.

The limitation of in-plane mechanical loadings can be solved by introducing equivalent stresses [15], [27], [28], [29]. Based on a simplified multiscale approach, an equivalent stress is presented in [30]. In this case, an equivalence in magnetization under multiaxial and uniaxial magneto-elastic loadings is proposed. By combining this strategy with the Jiles–Atherton–Sablik model [23], the effect of the magneto-mechanical coupling on the torque and losses of an electromagnetic device is evaluated in [31]. The main drawback of the equivalent stress of [30] is that it neglects the effects of shear with respect to the magnetic field. This limitation is addressed in [32], where an equivalent stress based on a thermodynamic approach is presented.

Another method to evaluate the effects of multiaxial stress on magnetic behavior is the combination of anhysteretic magneto-mechanical models and magnetic hysteresis approaches. Magneto-mechanical extensions of the Jiles–Atherton model are presented in [33], [34], and [35]. In the propositions of [34] and [35], simplified multiscale approaches are used to model the anhysteretic behavior, and the pinning parameter is adapted to the magneto-mechanical case. These coupled extensions allow estimating the losses of electrical machines subject to multiaxial stress loadings.

Manuscript received 4 May 2023; revised 18 July 2023; accepted 12 August 2023. Date of publication 28 August 2023; date of current version 24 October 2023. Corresponding author: L. G. da Silva (e-mail: luiz.dasilva@geeps.centralesupelec.fr).

Color versions of one or more figures in this article are available at <https://doi.org/10.1109/TMAG.2023.3309154>.

Digital Object Identifier 10.1109/TMAG.2023.3309154

A magneto-elastic extension based on the Hauser hysteresis model is proposed in [20], where a simplified multiscale approach models the reversible behavior. The model captures the trends for the evolution of the coercive field under biaxial stress. However, the definition of the irreversible field in the Hauser approach only allows uniaxial magnetic loadings. This is a strong limitation in predicting the magnetic behavior under a rotating magnetic field.

A recently published article [36] presents an extension of a hysteresis vector-play model to consider magneto-elastic loadings. This thermodynamically consistent model reasonably predicts the hysteresis behavior under uniaxial stress and shows promising results in representing asymmetric minor loops. The model allows for a multiaxial stress state and a vector magnetic loading, despite limitations to represent hysteresis losses under a rotating field of high intensity [37]. However, it has only been validated so far under uniaxial magneto-elastic conditions. A similar vector model is proposed in [38] considering the superposition of scalar play models. In this case, the hysteresis mechanism is evaluated at the grain scale, and the dissipation parameter is weighted by the volume fraction, which results in a parameter identification with stress-free measurements only. However, the hysteresis evaluation at the grain scale may increase the computational cost compared to the hysteresis mechanism applied directly at the macroscopic scale [36]. This difference can be crucial for finite-element simulation of devices.

In this article, the magnetic response of a NO Fe–Si steel under a multiaxial mechanical state is simulated using the vector-play model of [36]. In contrast with [36], where a simplified multiscale model was shown to appropriately represent the reversible behavior of a DC04 steel, the crystallographic texture has a more significant role when analyzing the magnetic response of Fe–Si. Therefore, in this work, the anhysteretic behavior is modeled from a multiscale approach where the crystallographic texture is considered. Another difference from the model presented in [36] comes from the use of an equivalent stress accounting for shear stress effects [32]. The material parameters are identified from the uniaxial measurements presented in [21] and [39], and the losses prediction under biaxial stress is compared with the measurements of [21].

II. MODELING

A. Reversible Behavior

The reversible behavior is modeled using a multiscale approach [40]. In this case, four scales are defined (see Fig. 1): the magnetic domain scale (denoted by the index α), the grain or single-crystal scale (denoted by the index g), the polycrystal (macroscopic) or representative volume element (RVE) scale, and the structure scale. This article focuses on modeling the magneto-elastic behavior at the RVE scale, which is the appropriate scale to define the macroscopic constitutive law of the material.

An orthonormal vector basis $(\vec{e}_1, \vec{e}_2, \vec{e}_3)$ is defined, in which \vec{e}_1 is the RD, \vec{e}_2 the TD, and \vec{e}_3 the normal direction. The

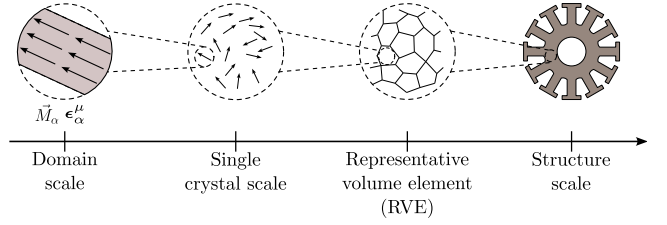


Fig. 1. Scales involved in the multiscale modeling.

magnetic field \vec{H} and mechanical stress σ are then written as

$$\vec{H} = \sum_i H_i \vec{e}_i \quad \text{and} \quad \sigma = \sum_i \sum_j \sigma_{ij} \vec{e}_i \otimes \vec{e}_j \quad (1)$$

where the operator \otimes represents the tensor product.

A domain family is defined as the set of domains with the same magnetization \vec{M}_α and magnetostriction strain ϵ_α^μ . In a domain family α with orientation $\vec{\alpha}$, the magnetization \vec{M}_α is

$$\vec{M}_\alpha = M_s \vec{\alpha} \quad \text{with} \quad \vec{\alpha} = \sum_i \alpha_i \vec{e}_i. \quad (2)$$

M_s is the saturation magnetization. The magnetostriction strain ϵ_α^μ for a cubic symmetry is written as

$$\epsilon_\alpha^\mu = \frac{3}{2} \begin{bmatrix} \lambda_{100}(\alpha_1^2 - \frac{1}{3}) & \lambda_{111}\alpha_1\alpha_2 & \lambda_{111}\alpha_1\alpha_3 \\ \lambda_{111}\alpha_2\alpha_1 & \lambda_{100}(\alpha_2^2 - \frac{1}{3}) & \lambda_{111}\alpha_2\alpha_3 \\ \lambda_{111}\alpha_3\alpha_1 & \lambda_{111}\alpha_3\alpha_2 & \lambda_{100}(\alpha_3^2 - \frac{1}{3}) \end{bmatrix} \quad (3)$$

with λ_{100} and λ_{111} being the magnetostriction constants. The components of $\vec{\alpha}$ and ϵ_α^μ in (2) and (3) are expressed in the crystal coordinate system, respectively.

From the energy balance at the domain scale and considering \vec{H} and σ homogeneous within the material, the Gibbs free energy density g_α is introduced. This energy density is composed of the sum of the magnetic g_α^{mag} , anisotropy g_α^{an} , and elastic g_α^{el} parts, defined as [40]

$$\begin{aligned} g_\alpha^{\text{mag}} &= -\mu_0 \vec{H} \cdot \vec{M}_\alpha \\ g_\alpha^{\text{an}} &= K_1(\alpha_1^2\alpha_2^2 + \alpha_1^2\alpha_3^2 + \alpha_2^2\alpha_3^2) + K_2(\alpha_1^2\alpha_2^2\alpha_3^2) \\ g_\alpha^{\text{el}} &= -\sigma : \epsilon_\alpha^\mu \end{aligned} \quad (4)$$

where K_1 and K_2 are the magneto-crystalline anisotropy constants. The operator \cdot is the dot product, and the operator $:$ is the double-dot product. The operations are evaluated with the quantities in the same coordinate system.

The volume fraction p_α of the domain family α is established by using a Boltzmann relation [41]

$$p_\alpha = \frac{\exp(-A_s g_\alpha)}{\sum_\alpha \exp(-A_s g_\alpha)} \quad (5)$$

where A_s is a material parameter. The set of possible domain family orientations is defined through the nodes of an icosphere—a geometric mesh that approximates a sphere using triangular faces [42]. In this work, an icosphere with 2562 nodes is used to represent the set of possible domain orientations.

With the definition of p_α , the magnetization \vec{M}_g , and the magnetostriction strain ϵ_g^μ at the grain scale are evaluated by

$$\vec{M}_g = \sum_{\alpha} p_{\alpha} \vec{M}_{\alpha} \quad \text{and} \quad \epsilon_g^\mu = \sum_{\alpha} p_{\alpha} \epsilon_{\alpha}^\mu. \quad (6)$$

The macroscopic (see RVE in Fig. 1) magnetization \vec{M} and magnetostriction strain ϵ^μ are then evaluated by an operation of volume average

$$\vec{M} = \sum_g p_g \vec{M}_g \quad \text{and} \quad \epsilon^\mu = \sum_g p_g \epsilon_g^\mu \quad (7)$$

where p_g represents the proportion of each grain orientation, which can be defined from the texture measurements of the sample.

B. Irreversible Behavior

The irreversible behavior is modeled at the macroscopic scale employing an energy-based model in a vector-play form [36], [43]. Applying the hysteresis model at the macroscopic scale results in neglecting the grain-to-grain interactions. This choice is justified because the dissipation is due mainly to the interaction between domain walls and defects, and a random distribution of defects within the material is assumed so that the dissipation parameters do not depend on the direction. Anisotropy effects due to the material texture or induced by the mechanical stress are accounted for through the reversible behavior. This choice reduces the computational cost of the proposed approach, which can be used in numerical analysis tools.

The dissipation D is modeled using an analogy with a dry-friction mechanism as [43]

$$D = \mu_0 \kappa \|\dot{\vec{M}}\| \geq 0 \quad (8)$$

with κ being the pinning field, a positive scalar. κ can be described by a symmetric positive-definite matrix to consider the anisotropy [44]. However, such an approach would require measurements along RD and TD to characterize the anisotropy and identify the dissipation parameters. In this work, the anisotropic effects were considered sufficiently captured from the anhysteretic behavior.

In this energy-based approach, the magnetic field is defined as the sum of reversible \vec{H}_{rev} and irreversible \vec{H}_{irr} parts. \vec{H}_{irr} is related to D by [43]

$$D = \mu_0 \vec{H}_{\text{irr}} \cdot \dot{\vec{M}} \geq 0, \quad \text{with} \quad \vec{H}_{\text{irr}} = \vec{H} - \vec{H}_{\text{rev}}. \quad (9)$$

The analogy of the magnetic hysteresis with a dry-friction mechanism is illustrated in Fig. 2.

To model the first magnetization curve and minor loops, the pinning field κ can be represented by a discrete distribution [43]. In this case, the single dry-friction system of Fig. 2 is replaced by a series connection of cells. In Fig. 3, a structure with N dry-friction cells is presented.

In this multicell context, the magnetic field at each k -cell is defined as

$$\vec{H} = \vec{H}_{\text{rev}}^k + \vec{H}_{\text{irr}}^k. \quad (10)$$

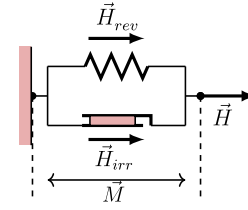


Fig. 2. Analogy of the magnetic hysteresis phenomena with a mechanical system.

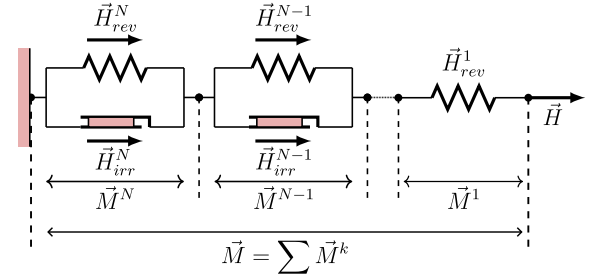


Fig. 3. Analogy of the magnetic hysteresis phenomena with a mechanical system made of N dry-friction cells.

From the mechanical analogy with a dry-friction system, and from the subdifferential of (8) in relation to $\dot{\vec{M}}$, the reversible field can be written as [43]

$$\vec{H}_{\text{rev}}^k = \begin{cases} \vec{H}_{\text{rev}(p)}^k, & \text{if } \|\vec{H} - \vec{H}_{\text{rev}(p)}^k\| \leq \kappa^k \\ \vec{H} - \kappa^k \frac{\vec{H} - \vec{H}_{\text{rev}(p)}^k}{\|\vec{H} - \vec{H}_{\text{rev}(p)}^k\|}, & \text{otherwise.} \end{cases} \quad (11)$$

with $\vec{H}_{\text{rev}(p)}^k$ being the previous value of the reversible field at the k -cell. The constant κ^k represents the pinning field at the k -cell. Due to the macroscopic approach considered for the hysteresis mechanism, there is no explicit connection between κ^k and the domain structure. The weight ω^k of each cell is introduced. It verifies

$$\sum_{k=1}^N \omega^k = 1. \quad (12)$$

The magnetization $\vec{M}^k(\vec{H}_{\text{rev}}^k, \sigma)$ and magnetostriction strain $\epsilon^{\mu,k}(\vec{H}_{\text{rev}}^k, \sigma)$ at each cell are evaluated considering the multi-scale approach presented in Section II-A. By using a weighted sum, the homogenized response is then

$$\vec{M} = \sum_{k=1}^N \omega^k \vec{M}^k(\vec{H}_{\text{rev}}^k, \sigma) \quad \text{and} \quad \epsilon^\mu = \sum_{k=1}^N \omega^k \epsilon^{\mu,k}(\vec{H}_{\text{rev}}^k, \sigma). \quad (13)$$

A simplified sketch of the algorithm is presented in Appendix A.

III. PARAMETERS IDENTIFICATION

The measurements performed on a NO Fe–Si electrical steel [21], [39] are used for the parameter identification. The discrete pole figures for the NO Fe–Si material are shown in Fig. 4. This set corresponds to 24 distinct crystallographic orientations with their corresponding volume fraction. The

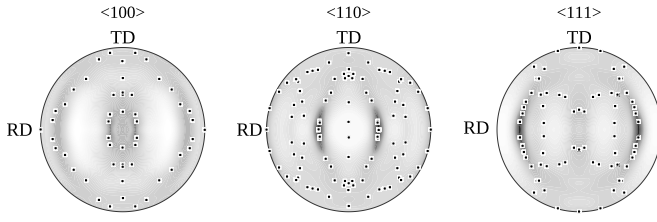


Fig. 4. Pole figures (24 orientations) for a NO Fe-Si alloy.

TABLE I

PARAMETERS OF THE REVERSIBLE MODELING

M_s (A/m)	λ_{100} (ppm)	λ_{111} (ppm)	K_1 (kJ/m ³)	K_2 (kJ/m ³)	A_s (m ³ /J)
$1.4 \cdot 10^6$	11.5	-4.5	38	0	$1.1 \cdot 10^{-2}$

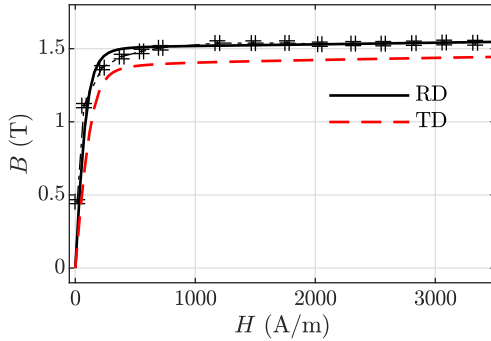


Fig. 5. Comparison between measured (error bars) and modeled (solid line) stress-free anhysteretic behavior along RD. The dashed line represents the prediction of the stress-free anhysteretic behavior along TD.

pole figures were obtained using the MTEX toolbox [45] from X-ray measurements reported in [46].

The measurements [21], [39] were performed considering in-plane stress assumption. Therefore, the stress tensor can be written in Voigt notation as

$$\sigma = [\sigma_{11} \ \sigma_{22} \ \sigma_{12}]. \quad (14)$$

The material parameters associated with the reversible behavior and the irreversible behavior are separately identified.

A. Reversible Behavior Parameters

The parameters λ_{111} , K_1 , and K_2 can be found in [47] for a Fe-Si material. Due to the simplifying assumptions to model the reversible behavior, the parameters M_s and λ_{100} are adapted for the modeling results to match with measurements of anhysteretic magnetization and magnetostriction strain for the stress-free case. The identified material parameters are listed in Table I.

The anhysteretic behavior for the stress-free case is presented in Fig. 5. The magnetization is oriented along RD and TD. The model satisfactorily reproduces the measured reversible behavior for the stress-free case with magnetization along RD. It is noted that anisotropic effects are more visible, especially above 1T.

Fig. 6 (top) presents the measured longitudinal (along RD) component of the magnetostriction strain with magnetic field and uniaxial stress applied in this same direction [39]. The

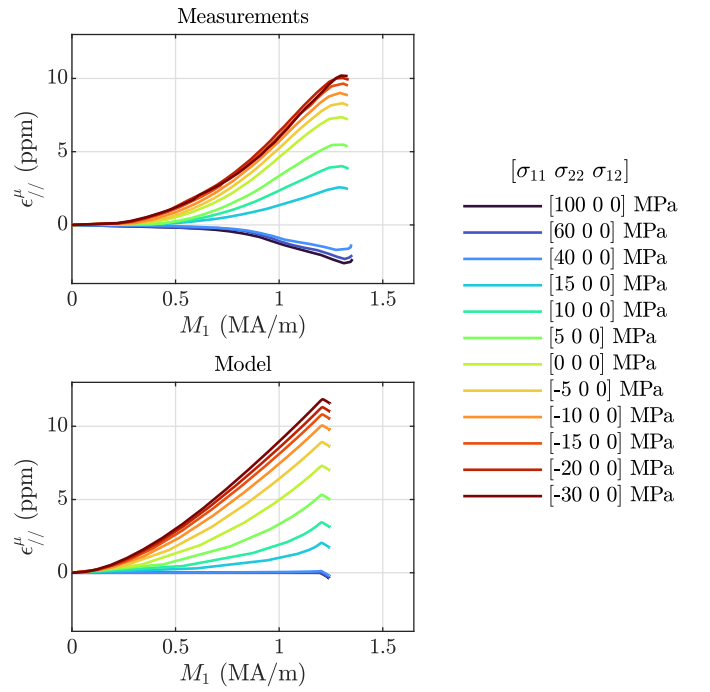


Fig. 6. Comparison between measured (top) [39] and modeled (bottom) magnetostriction strain along RD under uniaxial stress. Both magnetic field and stress are applied along RD. In-plane stress tensor in Voigt notation.

model [Fig. 6 (bottom)] captures both the trend under uniaxial stress and the rotation mechanism under a high field.

The measured magnetostriction [Fig. 6 (top)] is negative at high tension (above 15 MPa). This behavior can be attributed to the morphic effect [48], [49], in which a nonmonotonic behavior of magnetization and magnetostriction strain under stress occurs. A higher-order development of the magneto-elastic energy can reproduce this behavior in modeling [48], to the price of additional material parameters. However, this approach has limitations for modeling magnetostriction under high stress. Additional considerations on the magneto-elastic energy can be included to correct this drawback and are addressed in [49]. In this work, only the first-order development of the magneto-elastic energy is considered, which results in magnetostriction close to zero under high tension before the rotation mechanism.

B. Irreversible Behavior Parameters

The distribution $\omega(\kappa)$ can be identified based on the protocol presented in [50] and [51] for the stress-free case. For simulation purposes, the continuous distribution is discretized into 25 cells. More details about the identification procedure are presented in Appendix B.

From now on, the identified pinning field for the stress-free case will be denoted $\kappa^k(\mathbf{0})$. As proposed in [36], the evolution of the pinning parameter under stress can be defined as

$$\kappa(\sigma) = a(\sigma_{\text{eq}})\kappa^k(\mathbf{0}), \quad \text{with } a(\sigma_{\text{eq}}) = \frac{H_c(\sigma)}{H_c(\mathbf{0})} \quad (15)$$

with $a(\sigma_{\text{eq}})$ identified from uniaxial stress measurements of the coercive field H_c , and σ_{eq} is an equivalent stress. The effects

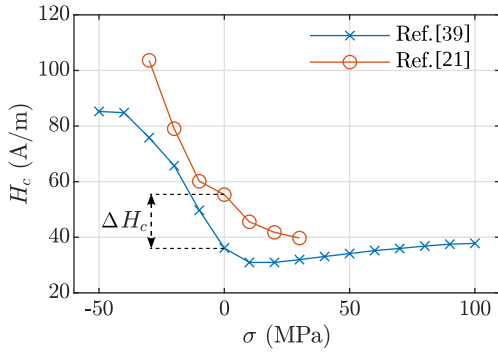


Fig. 7. Measured coercive field characteristic under uniaxial stress applied along RD for the setups presented in [21] and [39].

of shear with respect to the magnetic field are neglected in the equivalent stress of [30], previously considered in [36] to evaluate the coercive field evolution under uniaxial stress. In this work, the equivalent stress proposed in [32] is used, which allows modeling the influence of different shear modes on the coercive field. It is defined as

$$\sigma_{eq} = \begin{cases} r - \sqrt{\vec{e}^t \left(r\mathbf{I} - \frac{3}{2}\mathbf{d} \right)^2 \vec{e}}, & \text{if } \vec{e}^t \mathbf{d} \vec{e} \leq \frac{2r}{3} \\ r + \sqrt{\vec{e}^t \left(r\mathbf{I} - \frac{3}{2}\mathbf{d} \right)^2 \vec{e}}, & \text{otherwise} \end{cases} \quad (16)$$

with \vec{e} the unit vector that defines the direction of \vec{H} , \vec{e}^t the transpose operator, and \mathbf{I} the second-order identity tensor. Another material parameter to identify, r is the value of stress corresponding to the maximum permeability in a uniaxial configuration. \mathbf{d} is the deviatoric part of the stress tensor defined as

$$\mathbf{d} = \boldsymbol{\sigma} - \frac{1}{3} \text{tr}(\boldsymbol{\sigma})\mathbf{I} \quad (17)$$

with $\text{tr}(\boldsymbol{\sigma})$ being the trace operator. The material parameter r can be estimated from the permeability in the region around the coercive field. From the measurements of [39], r is identified as 10 MPa.

The measured coercive field evolution under uniaxial stress for both experimental setups [21], [39] is presented in Fig. 7. It can be noted that despite the common trend under stress, the results differ on the level of the coercive field. This can be attributed to differences in the preparation of samples for uniaxial and multiaxial tests. For example, in the multiaxial setup, the placement of the B-coil involves drilling holes in the sample. In this work, the measurements of the coercive field presented in [39] will be used for the identification of $a(\sigma_{eq})$ but shifted by ΔH_c —the coercive field difference for the stress-free case, to match with the experimental conditions of [21]. This choice is made because the measurements of [39] cover a wider range of stress levels.

The identification of $a(\sigma_{eq})$ is made by using the measurements along RD presented in [39] but shifted by ΔH_c . In the interpolation interval ($[-40, 100]$ MPa), $a(\sigma_{eq})$ is assumed as a piecewise linear function whose shape is presented in Fig. 8. Beyond the measurement range, we consider this function as

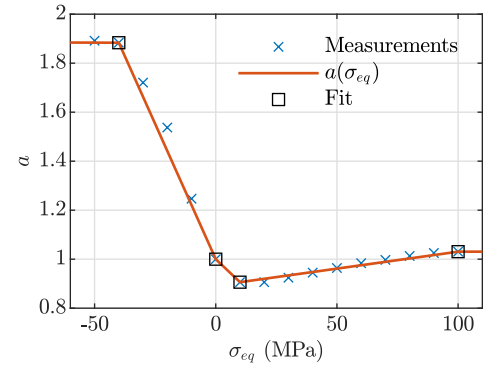


Fig. 8. Identified $a(\sigma_{eq})$ function from measurements along RD presented in [39] shifted according to [21]. The boxes indicate the experimental data used for the interpolation of $a(\sigma_{eq})$.

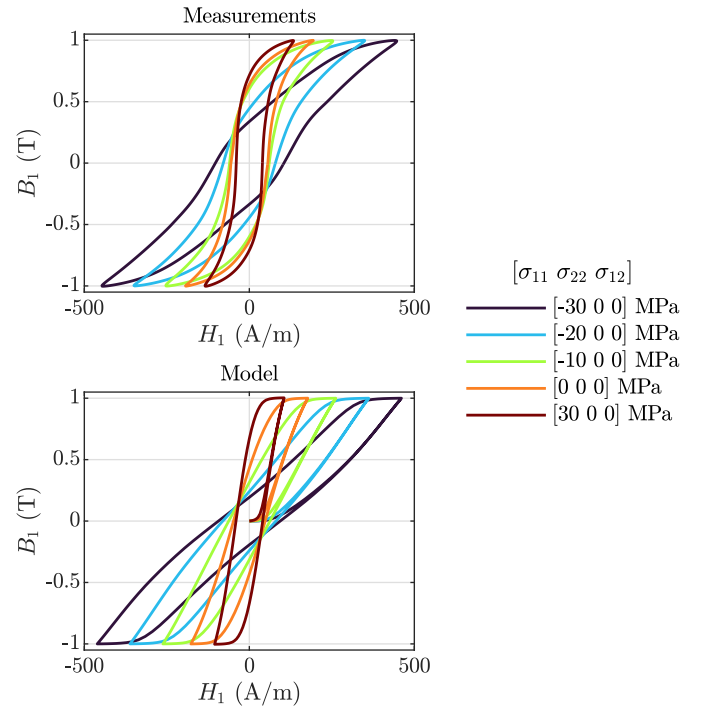


Fig. 9. Comparison between measured [21] (top) and modeled (bottom) hysteresis curves (at 1T) under uniaxial stress and field applied along RD. In-plane stress tensor in Voigt notation.

a constant with coercive field value defined by the maximum compression and the maximum tension cases.

IV. VALIDATION

A. Uniaxial Mechanical Stress

Considering the magnetic field and uniaxial stress applied along RD, in Fig. 9, the measurements presented in [21] are compared with the modeling results. The model captures the general trend under uniaxial stress. Differences are more evident when looking at the shape of the hysteresis loops, where it is a parallelogram format of the modeling results, especially in tension.

The model adequately reproduces the hysteresis losses when the uniaxial stress is applied either along RD or TD, as shown in Fig. 10.

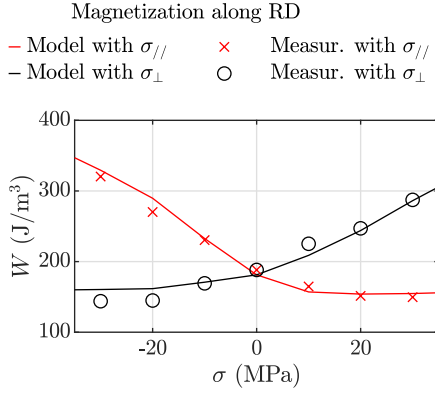


Fig. 10. Hysteresis losses (at 1T) with field applied along RD and under uniaxial stress. Measurements (markers) with stress along RD and TD [21] and modeling results (solid lines). In-plane stress tensor in Voigt notation.

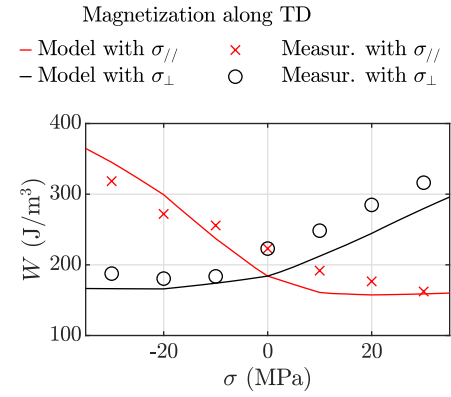


Fig. 12. Hysteresis losses (at 1T) with field applied along TD and under uniaxial stress. Measurements (markers) with stress along RD and TD [21] and modeling results (solid lines). In-plane stress tensor in Voigt notation.

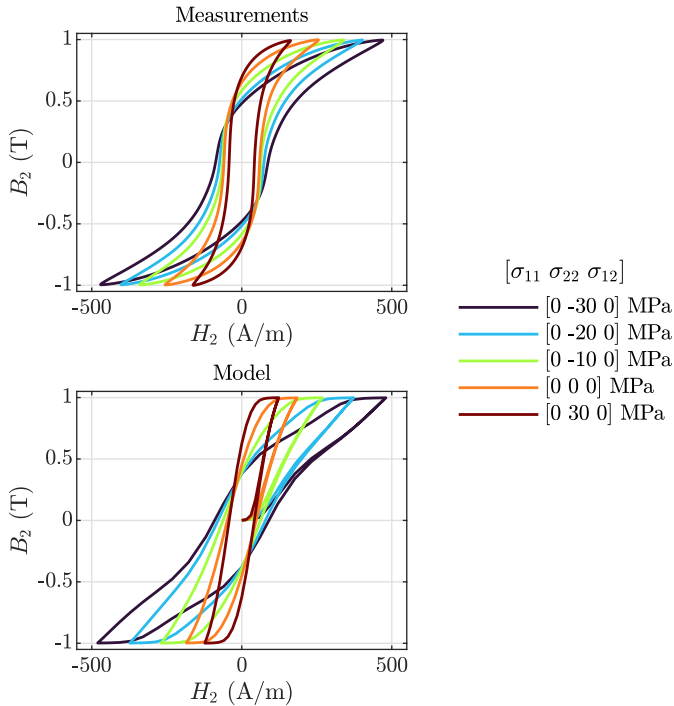


Fig. 11. Comparison between measured [21] (top) and modeled (bottom) hysteresis curves (at 1T) under uniaxial stress and field applied along TD. In-plane stress tensor in Voigt notation.

When the field and uniaxial stress are applied along TD, Fig. 11 shows the comparison between measurements [21] (top) and model (bottom). The definition of the pinning field as a function of equivalent stress allows capturing the evolution of the coercive field for this situation with field and stress applied along TD.

The hysteresis losses for the magnetic field applied along TD are presented in Fig. 12. Despite some differences (about 17% for 0 MPa), the model reasonably predicts the loss evolution when the uniaxial stress is applied either along RD or TD. It is important to note that the hysteresis parameters were identified by using measurements along RD. Therefore, this is a blind prediction test for which the model shows its

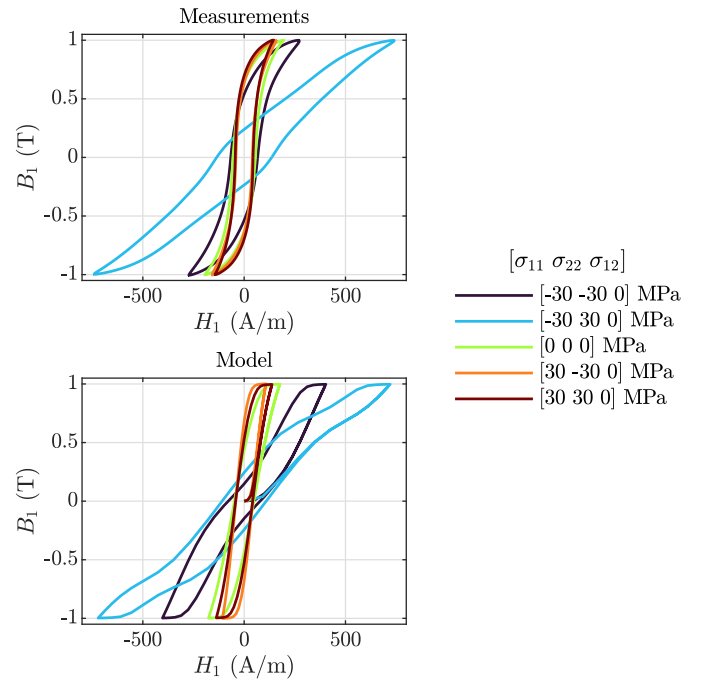


Fig. 13. Comparison between measured [21] (top) and modeled (bottom) hysteresis loops (at 1T) under biaxial stress with field applied along RD. In-plane stress tensor in Voigt notation.

capability to capture the tendency of losses under uniaxial loading.

V. MULTIAXIAL MECHANICAL STRESS

Considering a biaxial stress loading and the magnetic field applied along RD, the measured [21] hysteresis loops are presented in Fig. 13 (top). The modeling results in Fig. 13 (bottom) show that the model captures the degradation under shear. However, the modeled hysteresis loop under bi-compression presents curvatures that are not observed in the measurements. One hypothesis for this difference is that in the simplified approach presented here, the mechanical stress is taken as homogeneous in the polycrystal, which is not the case in a real material.

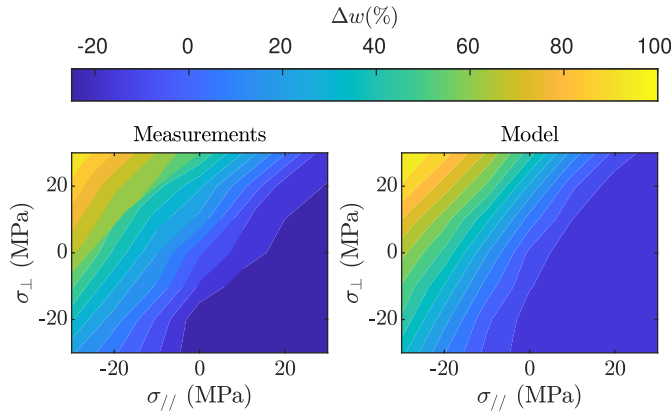


Fig. 14. Percentage variation of the hysteresis losses compared to the stress-free case at 1T. Magnetization along RD, and under biaxial stress. Measurements [21] (left) and model (right).

The variation of the hysteresis losses Δw due to the application of stress is evaluated by

$$\Delta w = \left[\frac{w([\sigma_{11} \ \sigma_{22} \ \sigma_{12}]) - w([0 \ 0 \ 0])}{w([0 \ 0 \ 0])} \right] 100 \quad (18)$$

where $w([0 \ 0 \ 0])$ and $w([\sigma_{11} \ \sigma_{22} \ \sigma_{12}])$ are the hysteresis losses for the stress-free case and under biaxial stress, respectively, in Voigt notation. Fig. 14 shows this percentage variation for both measurements [21] and model. Notably, the model captures the strong increase in hysteresis losses under shear when compression is applied along RD. Also, the model shows the tendency of a decrease in hysteresis losses under shear when traction is applied along RD.

The error e_{hyst} between measured w_{mes} and modeled w_{mod} hysteresis losses is evaluated as

$$e_{\text{hyst}} = \frac{w_{\text{mod}} - w_{\text{mes}}}{w_{\text{mes}}}. \quad (19)$$

This comparison indicator is presented in Fig. 15. Overall, the model is capable of modeling the hysteresis losses under biaxial stress, with main differences (around 15%) in the case of bi-compression. The difference in this biaxial configuration is explained because the model overestimates the degradation in the magnetization, as observed in Fig. 13 (bottom).

For a magnetic field applied along TD, the predicted hysteresis loops are presented in Fig. 16. Although the tendency of degradation under biaxial stress is captured, some differences are observed in the shape of the hysteresis loops. This is particularly problematic in the case of bi-tension.

Fig. 17 shows that the trend of hysteresis losses, compared to the stress-free case, is reasonably modeled. It is observed that shear (with compression applied along TD) increases the hysteresis losses of the material.

The error in the hysteresis losses between measurements and model is presented in Fig. 18. Important differences are seen, especially under bi-tension. For this loading, a significant difference in the modeled coercive field (about 25%) causes a large error in the simulated hysteresis losses.

The percentage variation of hysteresis losses with magnetization along RD and TD is shown in Fig. 19. This comparison indicator highlights the anisotropy effect. The modeling results

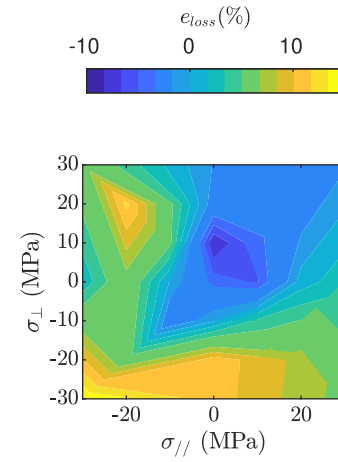


Fig. 15. Percentage error between measured and modeled hysteresis losses (at 1T) under magnetization along RD and biaxial stress.

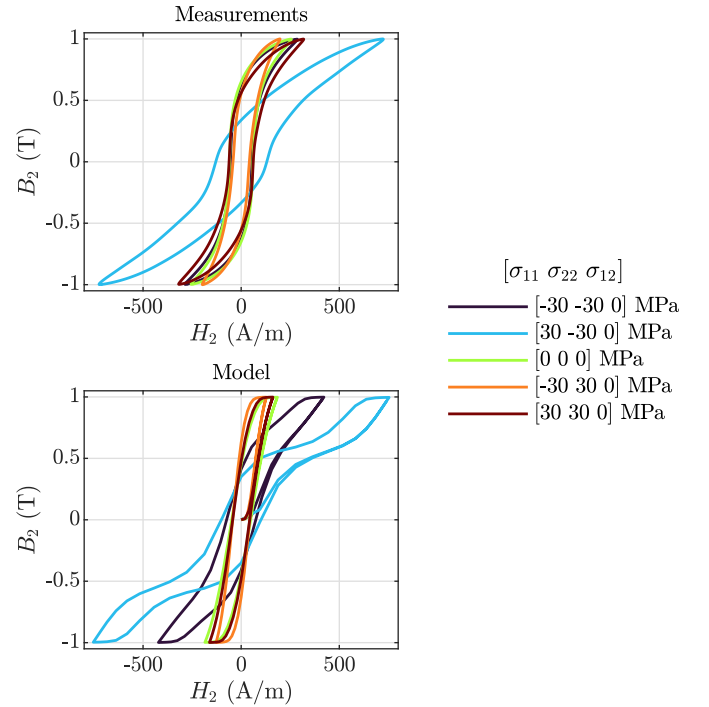


Fig. 16. Comparison between measured [21] (top) and modeled (bottom) hysteresis loops (at 1T) under biaxial stress with field applied along TD. In-plane stress tensor in Voigt notation.

exhibit less anisotropy than the measurements, especially in the case of bi-tension. Some factors may contribute to this significant difference, such as the value chosen for λ_{100} , the choice of the pinning parameter identified from measurements along RD only, or imperfections in the simplification of the texture. Moreover, as shown in Fig. 5, for maximum induction of 1T, the anisotropic effects are weak compared to higher induction levels.

The modeled magnetic response under the shear mode $\sigma = [0 \ 0 \ \sigma_{12}]$ and magnetization along RD is shown in Fig. 20 (bottom). It is noted that the model underestimates the degradation of magnetization, which is more evident in the measurements [21], especially under $\sigma_{12} = -30$ MPa.

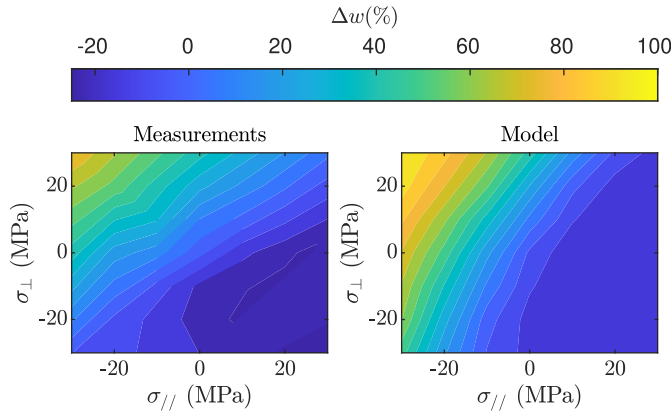


Fig. 17. Percentage variation of the hysteresis losses compared to the stress-free case at 1T. Magnetization along TD and under biaxial stress. Measurements [21] (left) and model (right).

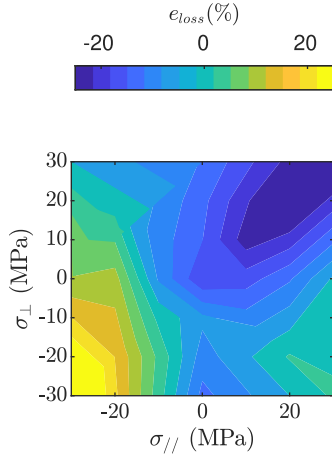


Fig. 18. Percentage error between measured and modeled hysteresis losses (at 1T) under magnetization along TD and biaxial stress.

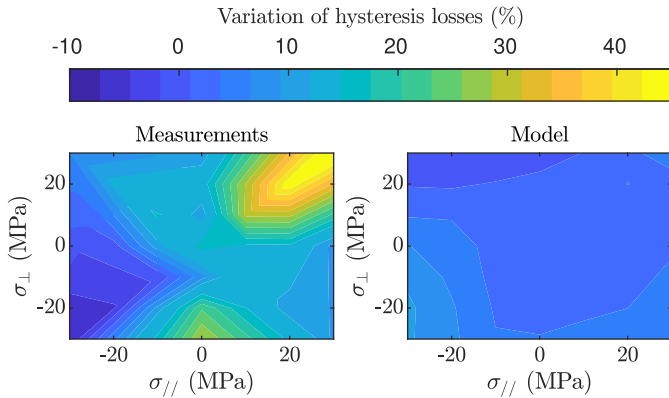


Fig. 19. Percentage variation of hysteresis losses with magnetization along TD compared to magnetization along RD.

The limitation of the model to represent the degradation under this shear mode results in important differences, particularly in the region of the remanent induction. Using the equivalent stress [32] allows capturing the evolution of the coercive field for this mechanical configuration, as observed in Fig. 21, for magnetization along RD or TD.

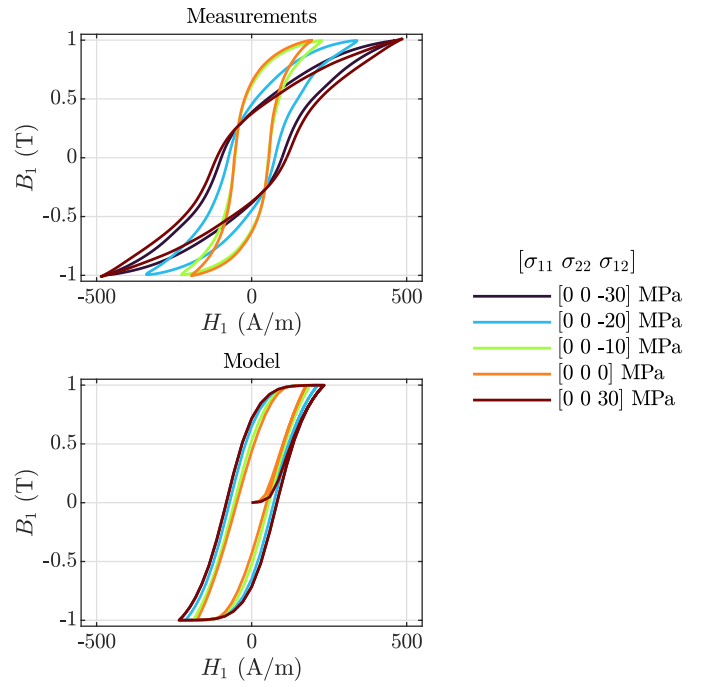


Fig. 20. Comparison between measured [21] (top) and modeled (bottom) hysteresis loops (at 1T) under shear with field applied along RD. In-plane stress tensor in Voigt notation.

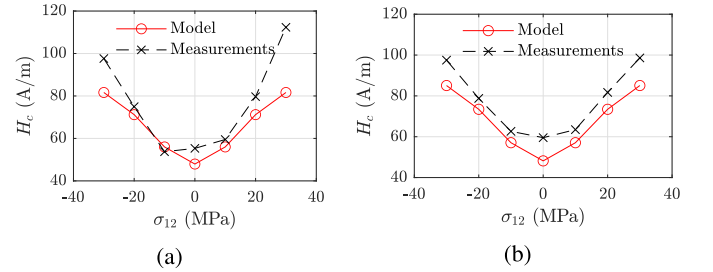


Fig. 21. Coercive field evolution at 1T under different levels of shear. (a) Magnetization along RD. (b) Magnetization along TD.

Fig. 22 presents the percentage variation of the losses compared to the stress-free case when the magnetization is along RD [Fig. 22(a)] and when the magnetization is along TD [Fig. 22(b)], both under shear. The model reproduces the trend of hysteresis losses increasing depending on the applied stress. However, the model overestimates the level of losses under this shear mode. Moreover, comparing Fig. 22(a) and (b) highlights the anisotropy of the material.

VI. CONCLUSION

In this article, an extension of a vector-play model under magneto-elastic loadings has been tested under biaxial stress conditions. A multiscale approach models the reversible behavior, in which homogeneous stress and magnetic field are considered at the RVE scale. Using parameters identified from uniaxial measurements along one direction only, the model captures the trend of the hysteresis losses under biaxial stress when the magnetization is along RD (with errors lower than 15%) or TD (with error lower than 25%). Considering the crystallographic texture, the anisotropic effects, even weak in

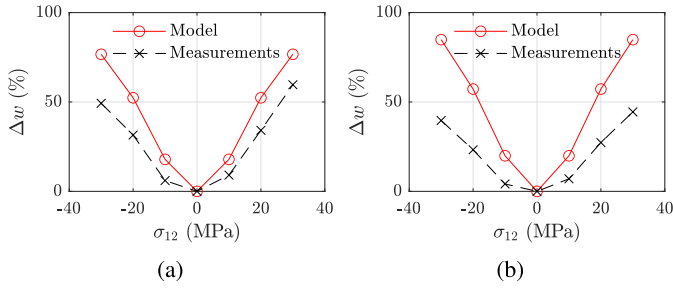


Fig. 22. Percentage variation of the hysteresis losses compared to the stress-free case at 1T under different levels of shear. (a) Magnetization along RD. (b) Magnetization along TD.

modeling, slightly change the magnetic response. The use of localization schemes in defining the magnetic field and stress at the grain scale could improve the modeling results, to the price of a significant increase in the simulation time. The proposed model is predictive because it can be applied to a more extensive range of mechanical stresses—inside the elastic limit—and amplitudes of induction than the ones used for parameter identification. The strategy presented in this work can be applied in the simulation of electrical machines subjected to a multi-axial stress state to have an optimal design of its ferromagnetic parts. Future works include the analysis of the model under a magneto-elastic loading with a rotating field.

APPENDIX A ALGORITHM OF THE MODEL

The main algorithm of the vector-play model is presented below. The subroutine MSM evaluates the reversible behavior. The parameters are described in Section II.

Algorithm 1 Algorithm of the Model

```

κ, ω, Ms, λ100, λ111, As, K1, K2; /* Mat. param. */
H, σ; /* Magneto-elastic loading */
0 ← Hrev(p); /* Initialization */
for k = 1 to N do
  if ||H - Hkrev(p)|| > κk then
    Hkrev ← H - κk  $\frac{H - H_{rev(p)}^k}{\|H - H_{rev(p)}^k\|}$ 
  else
    Hkrev ← Hkrev(p)
  end
  Mk, εμ,k ← MSM(Hkrev, σ, Ms, λ100, λ111, As, K1, K2)
  M ← M + ωkMk
  εμ ← εμ + ωkεμ,k
end

```

APPENDIX B PINNING FIELD PARAMETERS

For the identification of the distribution $\omega(\kappa)$, a set of measured coercive fields under several amplitudes of the

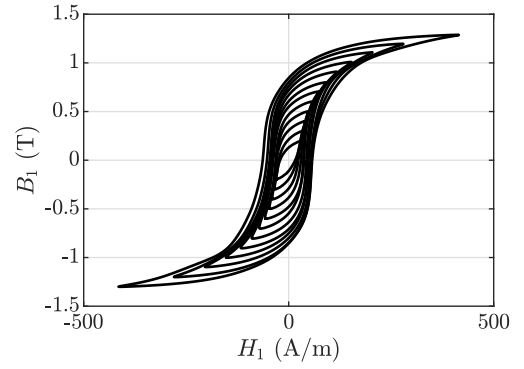


Fig. 23. Stress-free hysteresis loops under increasing magnetic field applied along RD.

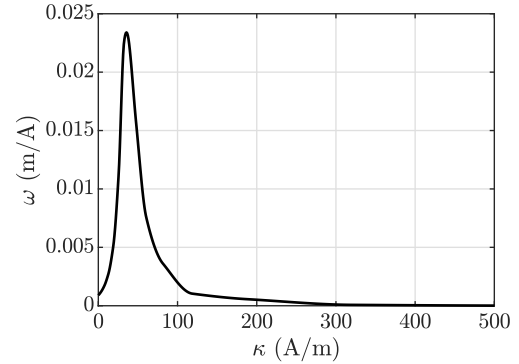


Fig. 24. Identified probability distribution for the stress-free case.

magnetic field is required [50]. The hysteresis loops used for the identification of $\omega(\kappa)$ are shown in Fig. 23 for applied field and measurements along RD. The identified pinning field distribution is presented in Fig. 24.

For numerical purposes, the continuous distribution presented in Fig. 24 is discretized as proposed in [50] into 25 cells.

ACKNOWLEDGMENT

This work was supported in part by the Brazilian Federal Agency for Support and Evaluation of Postgraduate Education (CAPES)/French Committee for the Evaluation of University and Scientific Cooperation with Brazil (COFECUB) under Project 88881.191763/2018-01. The work of Laurent Bernard was supported by the National Council for Scientific and Technological Development—(CNPq), and the work of A. Belahcen and F. Martin was supported by the Academy of Finland grant 346438.

REFERENCES

- [1] R. M. Bozorth, *Ferromagnetism*. New York, NY, USA: Van Nostrand, 1951.
- [2] B. D. Cullity and C. D. Graham, *Introduction to Magnetic Materials*. Hoboken, NJ, USA: Wiley, 2009.
- [3] A. Moses, "Effects of applied stress on the magnetic properties of high permeability silicon-iron," *IEEE Trans. Magn.*, vol. MAG-15, no. 6, pp. 1575–1579, Nov. 1979.
- [4] K. Ali, K. Atallah, and D. Howe, "Prediction of mechanical stress effects on the iron loss in electrical machines," *J. Appl. Phys.*, vol. 81, no. 8, pp. 4119–4121, Apr. 1997.

- [5] M. LoBue, C. Sasso, V. Basso, F. Fiorillo, and G. Bertotti, "Power losses and magnetization process in Fe-Si non-oriented steels under tensile and compressive stress," *J. Magn. Magn. Mater.*, vols. 215–216, pp. 124–126, Jun. 2000.
- [6] O. Perevertov, "Influence of the applied elastic tensile and compressive stress on the hysteresis curves of Fe-3% Si non-oriented steel," *J. Magn. Magn. Mater.*, vol. 428, pp. 223–228, Apr. 2017.
- [7] N. Leuning, S. Steentjes, M. Schulte, W. Bleck, and K. Hameyer, "Effect of elastic and plastic tensile mechanical loading on the magnetic properties of NGO electrical steel," *J. Magn. Magn. Mater.*, vol. 417, pp. 42–48, Nov. 2016.
- [8] M. B. S. Dias and F. J. G. Landgraf, "Compressive stress effects on magnetic properties of uncoated grain oriented electrical steel," *J. Magn. Magn. Mater.*, vol. 504, Jun. 2020, Art. no. 166566.
- [9] S. Zeze, Y. Kai, T. Todaka, and M. Enokizono, "Vector magnetic characteristic analysis of a PM motor considering residual stress distribution with complex-approximated material modeling," *IEEE Trans. Magn.*, vol. 48, no. 11, pp. 3352–3355, Nov. 2012.
- [10] H. Ebrahimi, Y. Gao, H. Dozono, K. Muramatsu, T. Okitsu, and D. Matsuhashi, "Effects of stress and magnetostriction on loss and vibration characteristics of motor," *IEEE Trans. Magn.*, vol. 52, no. 3, pp. 1–4, Mar. 2016.
- [11] K. Yamazaki and H. Takeuchi, "Impact of mechanical stress on characteristics of interior permanent magnet synchronous motors," *IEEE Trans. Ind. Appl.*, vol. 53, no. 2, pp. 963–970, Mar. 2017.
- [12] N. Takahashi, H. Morimoto, Y. Yunoki, and D. Miyagi, "Effect of shrink fitting and cutting on iron loss of permanent magnet motor," *J. Magn. Magn. Mater.*, vol. 320, no. 20, pp. e925–e928, Oct. 2008.
- [13] N. Boubaker, D. Matt, P. Enrici, F. Nierlich, and G. Durand, "Measurements of iron loss in PMSM stator cores based on CoFe and SiFe lamination sheets and stemmed from different manufacturing processes," *IEEE Trans. Magn.*, vol. 55, no. 1, pp. 1–9, Jan. 2019.
- [14] J.-W. Jung et al., "Mechanical stress reduction of rotor core of interior permanent magnet synchronous motor," *IEEE Trans. Magn.*, vol. 48, no. 2, pp. 911–914, Feb. 2012.
- [15] J. Pearson, P. T. Squire, M. G. Maylin, and J. G. Gore, "Biaxial stress effects on the magnetic properties of pure iron," *IEEE Trans. Magn.*, vol. 36, no. 5, pp. 3251–3253, 2000.
- [16] Y. Kai, Y. Tsuchida, T. Todaka, and M. Enokizono, "Influence of biaxial stress on vector magnetic properties and 2-D magnetostriction of a nonoriented electrical steel sheet under alternating magnetic flux conditions," *IEEE Trans. Magn.*, vol. 50, no. 4, pp. 1–4, Apr. 2014.
- [17] M. Rekić, O. Hubert, and L. Daniel, "Influence of a multiaxial stress on the reversible and irreversible magnetic behaviour of a 3%Si-Fe alloy," *Int. J. Appl. Electromagn. Mech.*, vol. 44, nos. 3–4, pp. 301–315, Mar. 2014.
- [18] Y. Kai, M. Enokizono, and Y. Kido, "Measurement of vector magnetic properties of a nonoriented electrical steel sheet under shear stress," *Electr. Eng. Jpn.*, vol. 191, no. 4, pp. 1–7, Jun. 2015.
- [19] U. Aydin et al., "Rotational single sheet tester for multiaxial magneto-mechanical effects in steel sheets," *IEEE Trans. Magn.*, vol. 55, no. 3, pp. 1–10, Mar. 2019.
- [20] L. Daniel, O. Hubert, and M. Rekić, "A simplified 3-D constitutive law for magnetomechanical behavior," *IEEE Trans. Magn.*, vol. 51, no. 3, pp. 1–4, Mar. 2015.
- [21] U. Aydin et al., "Effect of multi-axial stress on iron losses of electrical steel sheets," *J. Magn. Magn. Mater.*, vol. 469, pp. 19–27, Jan. 2019.
- [22] O. Hubert, Z. Maazaz, J. Taurines, R. Crepinge, F. van den Berg, and C. Celada-Casero, "Influence of biaxial stress on magnetostriction—Experiments and modeling," *J. Magn. Magn. Mater.*, vol. 568, Feb. 2023, Art. no. 170389.
- [23] M. J. Sablik and D. C. Jiles, "Coupled magnetoelastic theory of magnetic and magnetostrictive hysteresis," *IEEE Trans. Magn.*, vol. 29, no. 4, pp. 2113–2123, Jul. 1993.
- [24] M. J. Sablik, B. Augustyniak, and M. Chmielewski, "Modeling biaxial stress effects on magnetic hysteresis in steel with the field and stress axes noncoaxial," *J. Appl. Phys.*, vol. 85, no. 8, pp. 4391–4393, Apr. 1999.
- [25] M. J. Sablik and D. C. Jiles, "Modeling the effects of torsional stress on hysteretic magnetization," *IEEE Trans. Magn.*, vol. 35, no. 1, pp. 498–504, Jan. 1999.
- [26] S. E. Zirka, Y. I. Moroz, R. G. Harrison, and K. Chwastek, "On physical aspects of the jiles-atherton hysteresis models," *J. Appl. Phys.*, vol. 112, no. 4, pp. 1–7, Aug. 2012.
- [27] C. S. Schneider and J. M. Richardson, "Biaxial magnetoelasticity in steels," *J. Appl. Phys.*, vol. 53, no. 11, pp. 8136–8138, Nov. 1982.
- [28] K. Kashiwaya, "Fundamentals of nondestructive measurement of biaxial stress in steel utilizing magnetoelastic effect under low magnetic field," *Jpn. J. Appl. Phys.*, vol. 30, no. 11R, pp. 2932–2942, 1991.
- [29] M. J. Sablik et al., "Micromagnetic model for the influence of biaxial stress on hysteretic magnetic properties," *J. Appl. Phys.*, vol. 75, no. 10, pp. 5673–5675, May 1994.
- [30] L. Daniel and O. Hubert, "An equivalent stress for the influence of multiaxial stress on the magnetic behavior," *J. Appl. Phys.*, vol. 105, no. 7, Apr. 2009, Art. no. 07A313.
- [31] F. Martin et al., "Magneto-mechanical analysis of an axially laminated synchronous reluctance machine," in *Proc. XXII Int. Conf. Electr. Mach. (ICEM)*, Sep. 2016, pp. 1861–1867.
- [32] P. Rasilo, U. Aydin, F. Martin, A. Belachen, R. Kouhnia, and L. Daniel, "Equivalent strain and stress models for the effect of mechanical loading on the permeability of ferromagnetic materials," *IEEE Trans. Magn.*, vol. 55, no. 6, pp. 1–4, Jun. 2019.
- [33] T. Suzuki and E. Matsumoto, "Comparison of Jiles–Atherton and Preisach models extended to stress dependence in magnetoelastic behaviors of a ferromagnetic material," *J. Mater. Process. Technol.*, vol. 161, nos. 1–2, pp. 141–145, Apr. 2005.
- [34] L. Bernard and L. Daniel, "Effect of stress on magnetic hysteresis losses in a switched reluctance motor: Application to stator and rotor shrink fitting," *IEEE Trans. Magn.*, vol. 51, no. 9, pp. 1–13, Sep. 2015.
- [35] W. Zhao, S. Wang, X. Xie, X. Zhou, and L. Liu, "A simplified multiscale magneto-mechanical model for magnetic materials," *J. Magn. Magn. Mater.*, vol. 526, May 2021, Art. no. 167695.
- [36] L. G. D. Silva, A. Abderahmane, M. Domenjoud, L. Bernard, and L. Daniel, "An extension of the vector-play model to the case of magneto-elastic loadings," *IEEE Access*, vol. 10, pp. 126674–126686, 2022.
- [37] A. Bergqvist, "Magnetic vector hysteresis model with dry friction-like pinning," *Phys. B, Condens. Matter*, vol. 233, no. 4, pp. 342–347, Jun. 1997.
- [38] T. Matsuo, Y. Takahashi, and K. Fujiwara, "Anisotropic vector play model and its application in magnetization analysis," *IEEE Trans. Magn.*, vol. 59, no. 5, pp. 1–4, May 2023.
- [39] D. Singh, F. Martin, P. Rasilo, and A. Belachen, "Magnetomechanical model for hysteresis in electrical steel sheet," *IEEE Trans. Magn.*, vol. 52, no. 11, pp. 1–9, Nov. 2016.
- [40] L. Daniel, O. Hubert, N. Buiron, and R. Billardon, "Reversible magneto-elastic behavior: A multiscale approach," *J. Mech. Phys. Solids*, vol. 56, no. 3, pp. 1018–1042, Mar. 2008.
- [41] N. Buiron, L. Hirsinger, and R. Billardon, "A multiscale model for magneto-elastic couplings," *J. Phys. IV*, vol. 9, no. PR9, pp. 187–196, 1999.
- [42] L. Bernard, B. J. Mailhé, N. Sadowski, N. J. Batistela, and L. Daniel, "Multiscale approaches for magneto-elasticity in device simulation," *J. Magn. Magn. Mater.*, vol. 487, Oct. 2019, Art. no. 165241.
- [43] F. Henrotte, A. Nicolet, and K. Hameyer, "An energy-based vector hysteresis model for ferromagnetic materials," *COMPEL, Int. J. Comput. Math. Electr. Electron. Eng.*, vol. 25, no. 1, pp. 71–80, Jan. 2006.
- [44] L. Prigozhin, V. Sokolovsky, J. W. Barrett, and S. E. Zirka, "On the energy-based variational model for vector magnetic hysteresis," *IEEE Trans. Magn.*, vol. 52, no. 12, pp. 1–11, Dec. 2016.
- [45] F. Bachmann, R. Hielscher, and H. Schaeben, "Texture analysis with MTEX—Free and open source software toolbox," *Solid State Phenomena*, vol. 160, pp. 63–68, Feb. 2010.
- [46] F. Martin et al., "Analysis of the magneto-mechanical anisotropy of steel sheets in electrical applications," *IEEE Trans. Magn.*, vol. 56, no. 2, pp. 1–4, Feb. 2020.
- [47] D. Jiles, *Introduction to Magnetism and Magnetic Materials*. London, U.K.: Chapman & Hall, 1991.
- [48] O. Hubert, "Multiscale magneto-elastic modeling of magnetic materials including isotropic second order stress effect," *J. Magn. Magn. Mater.*, vol. 491, Dec. 2019, Art. no. 165564.
- [49] J. Taurines, B. Kolev, R. Desmorat, and O. Hubert, "Modeling of the morphic effect using a vanishing 2nd order magneto-elastic energy," *J. Magn. Magn. Mater.*, vol. 570, Mar. 2023, Art. no. 170471.
- [50] F. Henrotte, S. Steentjes, K. Hameyer, and C. Geuzaine, "Iron loss calculation in steel laminations at high frequencies," *IEEE Trans. Magn.*, vol. 50, no. 2, pp. 333–336, Feb. 2014.
- [51] K. Jacques, S. Steentjes, F. Henrotte, C. Geuzaine, and K. Hameyer, "Representation of microstructural features and magnetic anisotropy of electrical steels in an energy-based vector hysteresis model," *AIP Adv.*, vol. 8, no. 4, Apr. 2018, Art. no. 047602.